Individualized diversity in the extracellular metabolome of live human gliomas

Authors: Cecile Riviere-cazaux[1], Lucas P. Carlstrom[1], Karishma Rajani[1], Amanda Munoz-casabella[1], Jann N Sarkaria[2], Moses Rodriguez[3], Masum Rahman[1], Desmond Brown[3,7], Jaclyn F White[1], Samar Ikram[1], Alireza Shoushtarizadeh[1], Renee Hirte[1], Art Warrington[1,3], Ju-Hee H. Oh[8], William F. Elmquist[8], Rachael A Vaubel[4], Jeanette E Eckel-Passow[6], Sani H. Kizilbash[5], Terry C. Burns[1]

Institutions:
Departments of [1]Neurologic Surgery, [2]Radiation Oncology, [3]Neurology, [4]Pathology, [5]Oncology, and [6]Quantitative Health Sciences, Mayo Clinic, Rochester MN, USA

[7]Neurosurgical Oncology Unit, Surgical Neurology Branch, National Institutes of Neurological Disorders and Stroke, National Institutes of Health, Bethesda, MD, USA

[8]Brain Barriers Research Center, Department of Pharmaceutics, College of Pharmacy, University of Minnesota, Minneapolis, MN, USA

Corresponding Author Terry Burns, M.D., Ph.D.
Department of Neurosurgery – Mayo Clinic
200 First St SW
Rochester, MN, USA 55905
Burns.Terry@Mayo.edu

Keywords: Glioblastoma (GBM), oligodendroglioma, microdialysis, metabolomics, IDH

Abstract: Gliomas present a formidable challenge for translational progress. Heterogeneity within and between tumors may demand empirically individualized insights, though relatively little is known about the biochemical milieu within which malignant cells thrive in the *in vivo* human glioma. We performed a pilot study of intraoperative high molecular weight microdialysis to sample the extracellular tumor environment within three locations in each of five molecularly diverse human gliomas spanning WHO grade 2 oligodendroglioma to WHO grade 4 glioblastoma (GBM). Microdialysates were subjected to targeted (D/L-2-hydroxyglutarate (2-HG)) and untargeted metabolomic analyses, enabling correlation, clustering, fold change, and enrichment analyses. IDH-mutant tumor microdialysate contained markedly higher levels of D2-HG than IDH-wild type tumors. However, IDH status was not predictive of the global metabolomic signature. Rather, two distinct metabolic phenotypes (α and β) emerged, with IDH-WT and IDH-mutant patient samples in each group. Individualized metabolic signatures of enhancing tumor versus adjacent brain were conserved across patients with glioblastoma regardless of metabolic phenotype. Untargeted metabolomic analysis additionally enabled correlative quantification of multiple peri-operatively administered drugs, illustrating regional

heterogeneity of blood-brain barrier permeability. As such, acute intraoperative microdialysis affords a previously unharnessed window into individualized heterogeneous microenvironments within and between live human gliomas. Such access to the interstitial milieu of live human gliomas may provide a complementary tool for the development of individualized glioma therapies.

INTRODUCTION

Diffuse infiltrative gliomas include astrocytomas and oligodendrogliomas and comprise the majority of adult primary malignant brain tumors. While survival varies by grade and molecular subtype, all remain incurable regardless of the best available therapies. Glioblastomas (WHO grade 4 astrocytomas) are the most common and carry a median survival of 15 months (*1*). IDH mutations occur in all oligodendrocytomas and a subset of astrocytomas, affording improved prognosis due to typically slower growth and more favorable response to standard-of-care radiation and alkylating chemotherapy (*2, 3*). Highlighting the dismal rate of therapeutic progress, the last drug found to improve survival for gliomas was temozolomide in 2005 (*1*). Glioma heterogeneity among patients hampers therapeutic generalizations across diverse patient cohorts. Moreover, profoundly diverse genetic, epigenetic, and metabolic phenotypes accumulate within individual patients' tumor ecosystems (*4-6*). Such heterogeneity has hampered therapeutic efforts to target glioma-associated mutations. Conversely, divergent gliomas may nonetheless leverage convergent metabolic survival strategies in the setting of nutrient deprivation and genotoxic stress common across tumors (*7, 8*). As such, several features of glioma metabolism are increasingly viewed as promising therapeutic targets. Few strategies currently exist to characterize the metabolic landscape of *in vivo* human gliomas.

Microdialysis has been used to quantify human extracellular biomarkers of traumatic and hypoxic brain injury in neurocritical care units. Microdialysis is also a well-established method to quantify CNS drug delivery in early phase clinical trials (*9-12*). We here utilized high molecular weight (HMW) microdialysis catheters in a pilot feasibility study to determine whether the extracellular metabolic signatures at multiple sites within live human gliomas could be reliably evaluated intraoperatively prior to glioma resection. Twenty microliters (comprising a 10-minute sampling window) of microdialysate from each catheter conveyed multiple layers of data spanning tumor mutational status, radiographic localization, metabolic phenotype, and relative levels of multiple pharmacologic agents. Our findings provide evidence for both divergent and convergent metabolism within and between live human brain tumors and suggest that IDH status alone is insufficient to predict the global extracellular metabolic signature of live human gliomas.

RESULTS

Intraoperative microdialysis

Consented patients undergoing resection of gliomas underwent intraoperative placement of three high molecular weight (HMW; 100 kDA) microdialysis catheters into the tumor or

adjacent brain parenchyma (**Fig 1**). All catheters were placed within the planned resection volume prior to resection. In patients GBM^{mut}, $GBM^{WT}1$, $GBM^{WT}2$, enhancing tumor ("Enhancing") and brain adjacent to tumor ("Brain") were targeted, and a third catheter placed within non-enhancing tumor ("FLAIR"). Each patient with enhancing tumor was determined from pathology and molecular analysis to have a glioblastoma. Two patients (O^{II} and O^{III}) had large non-enhancing tumors that extended into adjacent eloquent language and motor regions requiring all catheters to be placed within the FLAIR+ tumor volume. Pathology for these patients demonstrated oligodendrogliomas. Microdialysis catheters (M dialysis) were perfused at 2uL/min with a 3% dextran solution. Aliquots were collected every 20 minutes and immediately frozen on dry ice. Clinical and technical details for each patient and catheter are provided in Supplemental Table 1. Analysis was performed using the second aliquot obtained following placement of catheters to avoid variable sample dilution from catheter dead volume.

The pathologic diagnosis for 4/5 patients was unknown at the time of surgery and was determined post-operatively by pathologic and molecular analysis of surgical specimens. One patient previously underwent surgery and chemoradiation for an IDH-mutant anaplastic astrocytoma a decade prior. Pathology demonstrated IDH-mutant glioblastoma (GBM^{mut}). This patient was discharged to inpatient rehabilitation prior to returning home. All other patients were discharged to home on post-operative day 2. No complications occurred. Intraoperative and postoperative management were not impacted by participating in the study.

Elevated D2-Hydroxyglutarate (D2-HG) in IDH-mutant tumor microdialysate

D2-HG is elevated in IDH-mutant gliomas and remains the best-characterized glioma oncometabolite. To determine if D2-HG levels in microdialysate are reflective of IDH status, we analyzed 10uL of microdialysate from each catheter for targeted analysis of D- and L-2-HG. D2-HG was elevated in microdialysate samples from IDH-mutant tumors (median: 27.29 µM, range: 9.59-831.80 µM) when compared to samples from IDH-wild type (WT) tumors (median: 0.63 µM, range: 0.22 µM-0.95 µM) (**Fig 2A**). Catheter B from patient GBM^{mut} had the highest recorded D2-HG level (831.80µM) and a >1000x lower level of D2-HG (0.68µM) when measured from adjacent brain (Catheter C). The adjacent brain in GBM^{mut} had levels of D2-HG comparable to that of catheters in patients with IDH-WT tumors. Intraoperatively collected CSF samples from patients O^{II}, GBM^{mut}, and $GBM^{WT}1$ were evaluated for D2-HG, yielding 3.186, 13.198, and 0.140 µM, respectively. Maximal extracellular tumor D2-HG as measured by microdialysis exceeded CSF D2-HG by as much as 9.3-fold in O^{II}. These data support the

feasibility of intraoperative HMW microdialysis to facilitate robust access and analysis of dialyzable tumor-associated extracellular metabolites from the tumor microenvironment.

To more comprehensively evaluate the extracellular glioma metabolome, a matching aliquot of each microdialysate sample was evaluated by untargeted metabolomic analysis using the Metabolon platform (*13*). Untargeted metabolomics cannot discriminate between the D- and L- stereoisomers of 2-HG. To directly compare the quantitative performance of the two platforms for a sample metabolite, we plotted the peak areas for 2-HG as measured by Metabolon to the total concentrations of D2-HG + L2-HG as quantified via targeted metabolomic analysis in CSF and microdialysate samples spanning a 2,500-fold concentration range. This analysis revealed a robust correlation (R^2=0.9989) between the two platforms (**Fig 2B)**, suggesting the potential for meaningfully quantitative comparisons between peaks identified via untargeted and targeted metabolomic analyses.

In total, 181 named metabolites yielded quantifiable peak areas in 15/15 catheters via untargeted metabolomic analysis (**Fig 4A).** Principal Component Analysis (PCA) was performed on the 15 catheter samples grouped according to IDH-status (IDH-mutant, n= 9, IDH wild-type, n=6) **(Fig 2C).** PCA was unable to separate IDH-mutant from IDH-WT samples; profound overlap of the two groups was seen in the 2-dimensional scores plot. However, supervised machine learning tools, including partial least squares-discriminant analysis (PLS-DA), sparse PLS-DA (sPLS-DA), and orthogonal projection to latent squares-DA (OPLS-DA) yielded separation of IDH-mutant samples from IDH-WT**.** As such, while 2-HG was confirmed as a dialyzable onco-metabolite of IDH-mutant glioma microdialysate, the overall extracellular metabolome was not fully explained by IDH status.

Individualized signatures of tumor versus brain enriched across patients

Two prior studies, both from the same group (*14, 15*), have previously reported a metabolic phenotype of glioblastoma microdialysate compared to that of adjacent brain. However, these studies were performed over several days, whereas our samples were collected acutely during surgery. Given the underwhelming IDH-associated metabolic phenotype, we asked if the intraoperative collection protocol was indeed compatible with detecting a tumor-associated phenotype beyond D2-HG. Three of the 5 patients had catheters placed in Enhancing (A), FLAIR (B), and adjacent brain (C) (**Fig 1C**). To identify the strongest possible comparative metabolic signature of tumor relative to the brain, we compared the metabolome of catheters A (tumor) and C (brain) for each of these three patients.

Given our long-term goal of leveraging metabolic feedback from individual patients, we compared the relative abundance of each quantified metabolite in catheter A vs C and generated ranked metabolite lists for each patient based on fold change. To quantify the relative similarity of the ranked metabolite lists between patients, we turned to a well-established rank-based enrichment algorithm more commonly utilized for gene-based enrichment analyses (Gene Set Enrichment Analysis, GSEA) and repurposed it for metabolomic analysis. We found that each comparison yielded at least 35 metabolites with a minimum 2.4 folder change (range: 2.4 to 122.39) between catheters A vs C. As such, we took the top and bottom 35 metabolites from each comparison and determined where these metabolites fell in the ranked gene lists for the remaining two patients using GSEA. Reassuringly, each patient's individual tumor signature was highly enriched in other patients' tumor signatures (**Fig 3A)** and not in the brain signature of other patients (**Fig 3B)**. Remarkably, based on data from a single patient, the degree of enrichment across unrelated individual patients proved highly robust in each case with a False Discovery Rate (FDR) of 0.0076 or less across each of 6 comparisons (**Fig 3C)**. Importantly, the metabolic signature of tumor versus adjacent brain from both previously published reports of the human glioblastoma microdialysate metabolome was strongly enriched in 3/3 patients with FDRs of 0.006 or less for Björkblom et al.(*15*) and FDRs of 0.013 or less for Wibom et al. (*14*) (**Fig 3C)**. Björkblom et al also reported a smaller number of 13 selectively brain-associated metabolites. This was significantly enriched in the comparative metabolome of only 1 of 3 patients in our data. Utilizing our own individualized comparative data between catheters A and C, we performed enrichment analysis for metabolites differentially abundant in catheter C and compared results across patients. Of six possible enrichment analyses, five revealed an FDR of 0.0, the 6th FDR was 1.08×10^{-4}. A reproducible signature of both brain and tumor appeared apparent based on individualized comparisons of brain and tumor. To determine if specific metabolites accounted for this enrichment, we asked which metabolites were consistently represented in the "leading edge" of enrichment across each individualized analysis. The most reproducible tumor-associated metabolites included guanidoacetic acid, as well as multiple amino acids and their derivatives. A distinct set of metabolites were reproducibly enriched in brain including N-Acetylaspartylglutamic acid (NAAG) and N-Acetylgalactosaminidase (NAGA) (**Fig 3D)**. Thus, with as few as 2 catheters in a single patient, a tumoral metabolic signature could be defined as distinct from brain. Repeating this analysis in 3 patients revealed 6 signatures, each of which was highly reproducible in both unrelated patients (12/12). As such, although we failed to identify a robust global metabolic signature differentiating IDH-mutant from IDH-WT glioma, intraoperative microdialysis appeared sufficient to reproducibly differentiate

tumor from brain and reproduce previously published signatures of human glioblastoma microdialysate.

Correlation and clustering analyses

Having validated the utility of intraoperatively acquired microdialysate to detect elevated 2-HG in IDH-mutant tumors and reproducibly discriminate tumor from brain, we next proceeded to evaluate global metabolomic signatures across the full cohort of 15 samples. To provide an overview of the metabolic data collected, Pearson correlation maps were generated based on the 181 consistently quantifiable metabolites based on hierarchical clustering between the detected metabolites (**Fig 4A)** and samples (**Fig 4B).** Samples from patients O^{II}, O^{III}, and $GBM^{WT}1$ each clustered separately by patient. However, for patients GBM^{mut} and $GBM^{WT}2$, catheters A (enhancing) and catheters C (brain) clustered together. Since the Pearson correlation analysis suggested overlap between the metabolic phenotype of patients GBM^{mut} and $GBM^{WT}2$, we asked if similar results would be obtained based upon clustering analyses (**Figure 4C).** Indeed, when the data was dimensionally reduced using PCA, samples from O^{II}, O^{III}, and $GBM^{WT}1$ began to cluster together, whereas samples from GBM^{mut} and $GBM^{WT}2$ were more dispersed from that group. Supervised analysis using sPLS-DA revealed complete separation of samples from O^{II}, O^{III}, and $GBM^{WT}1$. By contrast, all samples from $GBM^{WT}2$ clustered with samples from GBM^{mut}, but not O^{II}, O^{III}, and $GBM^{WT}1$ (**Figure 4D).** As such, both Pearson correlation analysis and clustering algorithms indicate that an IDH-WT ($GBM^{WT}1$ and $GBM^{WT}2$) and an IDH-mutant GBM (GBM^{mut}) could share an overlapping metabolic phenotype, hereafter termed "α," which was distinct from other IDH-mutant and IDH-WT gliomas, hereafter termed "β."

Dichotomized metabolic phenotype of tumor microdialysates

Given these emerging metabolic phenotypes, to visually compare the relative ability of IDH versus α/β designation to define a tumor's extracellular metabolic signature, hierarchical clustering heat maps were generated for tumor samples (n=12) to visualize the top 25 differentially abundant metabolites based on each classification. IDH-mutant versus IDH-wild type microdialysate samples failed to demonstrate an obviously consistent metabolic pattern separating groups (**Fig 5A).** By comparison, the hierarchical clustering heat map comparing α and β metabolic phenotypes revealed a clearly defined metabolic phenotype (**Fig 5B**).

Volcano plots were generated to determine the most statistically significant different metabolites separating each grouping strategy (IDH status and phenotypes α versus β). Nine metabolites were significantly higher in IDH-mutant samples ($p>0.05$) and 8 in IDH-WT samples (**Figure 5C)**. Among these, 2-HG (IDH-mutant/WT FC=63.148) and sorbitol (12.411) were elevated in IDH-mutant, and urocanic acid was higher in IDH-WT (0.066). By comparison, 61 metabolites discriminated phenotype α from β at log2FC >2 and $p<0.05$ (**Figure 5D)**. Fifty-six of these were higher in β, the top five of which (ranked by p-value) were threonic acid (α/ β FC= 0.118), oxalic acid (0.120), DMTPA (0.049), L-lyxonate (0.133), and creatinine (0.329). The five metabolites associated with the α phenotype were guanidoacetate (α/β F=37.345), propionylcarnitine (3.70), lenticin (3.04), L-asparagine (2.696), and L-alanine (2.103). Collectively, these data suggested the metabolic phenotype of α versus β subtype gliomas microdialysate samples to be more metabolically divergent than IDH-WT vs IDH-mutant microdialysate samples.

Metabolic phenotypes are distinct, but certain metabolites are preserved

Having established which metabolites differentiated α from β, we next sought to determine which metabolites may discriminate tumor from brain in α and β tumors, respectively. FOlc change analysis comparing α (n=4) and β (n=8) each to brain (n=3) revealed 21 metabolites higher in α than brain and 70 metabolites in β (**Figure 6B-C**). Fifteen metabolites were shared between the two comparisons (**Figure 6D).** Those with the lowest p values unique to β versus brain were threonic acid, myo-inositol, and oxoglutaric acid. Unique to α versus brain, the most significant metabolites were L-phenylalanine, D-lysine, and L-asparagine.

One of the most clinically pertinent classifications of infiltrative gliomas is between astrocytomas and oligodendrogliomas. In our cohort, all astrocytomas were WHO grade 4 (GBM). Both patients with an α metabolic phenotype had GBMs, whereas the β phenotype included a patient with a GBM and two with oligodendrogliomas. Consistent with this metabolically diverse cohort of GBMs in our cohort, only 3 metabolites were found which were unique to astrocytomas; these were propionylcarnitine (glioma/oligodendroglioma FC = 5.698), trigonelline (3.839), and L-carnitine (2.180). However, 25 metabolites were uniquely abundant in the microdialysate of oligodendrogliomas versus GBMs. The three most significant metabolites differentiating oligodendrogliomas from astrocytomas were methylsuccinic acid, (Glioma/Oligo FC = 0.380), L-lyxonate (0.232), and mannonic acid (0.285).

Pathway analysis

To evaluate what differential biological processes may underlie the observed differentially abundant metabolites, enrichment analysis was performed for catheter C (brain) vs catheter A (tumor) in each patient (**Supp Fig 1)**. Microdialysate from GBMs was uniformly enriched for aminoacyl-tRNA biosynthesis and valine, leucine, and leucine biosynthesis and degradation ($p<0.05$). Oligodendroglioma samples were differentially enriched for various metabolic pathways, such as arginine and proline metabolism in O^{II} and phenylalanine metabolism in O^{III} ($p<0.05$). As such, oligodendrogliomas and astrocytomas have unique metabolomic features, but these do not fully explain the patient's tumor metabolome because of $GBM^{WT}1$'s metabolic signature grouping with O^{II} and O^{III} in phenotype β.

Microdialysate reflects the intraoperative story

Within the 315 named metabolites identified in untargeted analysis, several drugs and their metabolic derivatives were present. Patients routinely receive certain drugs such as levetiracetam (Keppra), cefazolin (Ancef), and mannitol peri-and intraoperatively.

Keppra is a CNS-penetrant anti-epileptic medication routinely administered prior to tumor resection to minimize risk of seizures, barring known allergies or intolerance. Consistent with this, Keppra was detected in 3/3 microdialysate samples from each of four patients; no Keppra was detected in any samples from patent O^{III} (**Fig 7A).** Indeed, review of the medical record confirmed that Keppra was not administered to patient O^{III} due to a documented Keppra allergy. Given that Keppra is reported to be CNS penetrant, we were interested to note that Keppra levels varied by as much as 2x within individual patients. While relatively high levels were observed in catheter A (enhancing tumor) for the three patients with GBM, the highest levels were observed in catheter B for GBM^{mut} and O^{II}. This may suggest that variable BBB disruption (expected in GBM catheters A only) does not fully explain the relative Keppra distribution within patients. Alternatively, catheters may vary in their relative levels of recovery across different areas of the brain. Given that a 15-metabolite signature was available to discriminate tumor from brain across α and β tumor phenotypes (**Fig 6D)**, we leveraged this signature to ask if local Keppra levels may correlate with the relative tumor burden at each catheter site. To address this question, the relative levels of the 15 metabolites were evaluated via heatmap across all 15 catheter samples (**Supp Fig 2**). Indeed, this analysis suggested that Catheter B ("FLAIR") more closely resembled "Brain" than "Enhancing" tumor in the IDH-WT GBMs ($GBM^{WT}1$ and $GBM^{WT}2$), whereas Catheter B in GBM^{mut} more closely resembled enhancing tumor than brain. Keppra levels conformed to this general pattern. Moreover, in Patient O^{II}, wherein all catheters were placed within FLAIR, a greater tumoral signal was

present in Catheter B, in agreement with a relatively higher Keppra level in Catheter B. As such, relative Keppra levels within both enhancing and non-enhancing human gliomas may correlate positively with relative tumor burden. If true, Keppra levels could conceivably parallel those more subtle alterations in cerebrovascular function that are themselves responsible for the radiographic appearance of vasogenic edema.

Cefazolin (Ancef) is administered as a pre-operative antibiotic and has poor CNS penetration. High-grade gliomas can result in degradation of the blood-brain-barrier (BBB), as exemplified by areas of contrast enhancement on gadolinium-enhanced MRIs. Consistent with this, Ancef was only identified in microdialysate from two catheters, both of which were placed in regions of contrast enhancing tumor in patients with glioblastoma. The third patient with glioblastoma was not administered Ancef due to a documented allergy (**Fig 7B).** Importantly, the failure to recover any quantifiable Ancef in the microdialysate of 10/10 catheters placed outside of enhancing tumor suggests that intraoperative placement of microdialysis catheters does not cause sufficient disruption of the BBB to enable robust detection of a CNS non-penetrant drug.

Mannitol is often administered intraoperatively to mitigate cerebral edema and brain swelling. Mannitol was only administered to patients O^{II} and GBM^{mut}; mannitol peak areas were higher across all three catheters in these two patients when compared to those who were not administered mannitol (**Fig 7C)**. Within these patients, the pattern of mannitol followed that of Keppra, being highest in regions of elevated tumor burden. That a measurable amount of mannitol crosses the non-disrupted BBB reinforces the principle that its continuous administration will predicably decrease its efficacy over time. Nevertheless, it is interesting to note that the mannitol to Keppra ratio was lower in GBM^{mut} than O^{II}. Although a time-course analysis was not performed, mannitol was administered more than 2 hours prior to microdialysis in patient GBM^{mut} but concurrent with initiation of microdialysis in patient O^{II}. As such, it is tempting to speculate that the short plasma half-life (2h) of mannitol accounted for its relatively lower CNS level in patient GBM^{mut} than O^{II}. Additional drugs administered prior to or during surgery include 5-ALA for fluorescent visualization of high-grade tumor, caffeine (administered to certain patients during awake surgery) and acetaminophen. No named metabolite corresponding to 5-ALA was identified in the Metabolon data. However, the highest levels of both caffeine and acetaminophen, were identified in patients who received these drugs during surgery, with relative levels of drug and metabolites thereof correlating with time of administration (**Supp Fig 3**). Collectively, these data suggest that acute intraoperative microdialysis paired with UPMS-MS may provide an efficient avenue to assess relative CNS

levels of at least 5 intraoperatively administered pharmacologic agents across multiple tumor regions in concert with focal analysis of local tumor phenotype and burden.

DISCUSSION

We tested the feasibility of intraoperative microdialysis to evaluate the extracellular metabolome within live human gliomas immediately prior to resection. Leveraging this previously untapped window of opportunity, we demonstrate: 1) robustly elevated D2-HG in IDH-mutant glioma microdialysate; 2) a dichotomy between global metabolic phenotypes not driven by IDH status that we term α versus β; 3) individualized metabolic signatures of enhancing glioblastoma versus adjacent brain that are significantly conserved across individuals with diverse tumors; and, 4) concurrent intratumoral analysis of at least 5 different intraoperatively administered drugs across multiple regions of live human glioma.

Intraoperative microdialysis: a convenient and robust window into tumor metabolism

Increasing preclinical evidence suggests the potential therapeutic utility of targeting cancer-associated metabolic vulnerabilities. In contrast to the profound genomic heterogeneity seen within and across malignancies, a more finite set of convergent metabolic strategies might be deployed to meet the unique bioenergetic demands of a tumor. These enable tumor survival and proliferation in the face of genomic instability, oxidative stress, hypoxia and nutrient deprivation. Improved experimental windows into live human tumor metabolism are needed to support individualized medicine and drug development efforts targeting metabolic vulnerabilities within cancers. Magnetic Resonance Spectroscopy (MRS) can noninvasively evaluate certain metabolites and candidate pharmacodynamic biomarkers with anatomic resolution(*16*). However, technically demanding protocols still under development currently require dedicated teams with unique expertise. Reliable detection via MRS of D2-HG--the most robust known glioma oncometabolite—has remained elusive at most academic centers. One recent intraoperative study compared the metabolomic profile of venous blood draining live gliomas during surgery to peripheral venous blood (from the foot), normalizing each against arterial blood (*17*). However, no conclusions could be made regarding differential metabolism of tumor versus brain. Conversely, intraoperative microdialysis enabled comparative metabolic analysis across variably tumor-infiltrated regions within the brain of individual patients prior to resection. Importantly, commercially available microdialysis catheters can be easily and safely placed within desired brain or tumor regions by any tumor surgeon during clinically indicated surgical

procedures; transportable aliquots can be kept frozen and analyzed off-line, decreasing requirements for local expertise.

IDH status versus global metabolic phenotype

IDH-mutant gliomas epitomize the oncogenic relevance of altered metabolism. The pathologic accumulation of high D2-HG levels in IDH-mutant gliomas induces hypermethylation of cytosine-phosphate-guanine (CPG) islands, compensatory changes in glutaminolysis, and disruption of de novo lipogenesis (*18*). MGMT hypermethylation in IDH-mutant GBMs impedes DNA repair, improving response to standard cytotoxic therapy (median survival 31 months versus 15 months in IDH-wild type) (*2*), while methylation of other genes, such as NAPRT, may reveal untapped metabolic vulnerabilities (*19*). We found elevated D2-HG in the CSF and microdialysate in IDH-mutant tumors (Fig 3); microdialysate consistently yielded up to 60-fold higher D2-HG relative to CSF, highlighting the potential value of measuring candidate metabolic biomarkers directly at the source. Interestingly, the low D2-HG in GBM^{mut} Catheter C suggests a potentially shorter distance of D2-HG diffusion than previously estimated based on computational modeling (*20*). This observation could empower future studies monitoring D2-HG in response to focally delivered therapies. D2-HG was previously used as a pharmacodynamic biomarker for IDH inhibitors in tissue (*21*) and via MRS (*22-24*). Paired targeted and untargeted analysis of microdialysate enabled us to interpret D2-HG levels in the context of a global metabolic phenotype, revealing an unexpected discordance between IDH status and the global metabolic phenotype.

Samples from GBM^{mut} and $GBM^{WT}2$ varied clinically and technically. GBM^{mut} recurred from an anaplastic IDH-mutant astrocytoma treated with chemoradiation 10 years prior. Surgery was performed asleep with a lactated ringer (LR)-based perfusion fluid with dextran 40. Conversely, $GBM^{WT}2$ was newly diagnosed IDH-WT GBM with samples obtained during awake surgery with LR-free perfusion fluid including dextran 500. Despite these multiple differences, microdialysate samples clustered together, suggesting some degree of convergent evolution to a phenotype we referred to as phenotype α. Similarly, we were surprised to find that $GBM^{WT}1$ clustered in-between O^{II} and O^{III} by PCA within phenotype β. As such, while D2-HG may be a viable biomarker for IDH-mutant tumors, alternate metabolic alterations may more completely define the overall tumor metabolome of glioblastoma. At present, all five participants are alive without recurrence arguing against either phenotype imparting an atypically poor prognosis (median follow-up = 17.7 months, range: 7.1-18.6 months). Nevertheless, the divergent

metabolic phenotypes within both IDH-mutant and IDH-WT gliomas may highlight opportunities for individualized metabolically targeted therapies. It is important to note that each catheter in this study was analyzed as a unique sample source, with patient identity comprising one of multiple variables. Although signatures of enhancing tumor versus adjacent brain from individual patients were strongly enriched between patients and across prior studies (*14, 15*), identified metabolites within the metabolic phenotypes at this point should be regarded as illustrative and hypothesis generating observations rather than candidate biomarkers given the very small sample size. Moreover, metabolite set enrichment analysis for the enhancing tumor-associated metabolites yielded enrichment only for aminoacyl-tRNA biosynthesis, and valine, leucine and isoleucine biosynthesis and degradation. As such, further studies will be needed to annotate metabolic pathways differentially enriched within and between defined tumor microdialysates.

Concurrent pharmacologic analyses

We had not originally planned to quantify pharmacologic agents. However, five intraoperatively administered drugs matched profiles from the Metabolon library, enabling relative quantifications. The absence of Ancef and Keppra in patients with allergies supports the specificity of findings for these drugs. Interestingly, the absence of Ancef (a non-CNS-penetrant drug) from all catheters placed outside of enhancing tumor suggests the feasibility of acute intraoperative microdialysis without marked disruption of the blood brain barrier. Since these were not part of the original experimental design, these pharmacologic agents are hampered by lack of correlative levels in systemic circulation, lack of quantitative standards, and absence of time-course analyses. For example, mannitol is considered non-CNS penetrant, but was detected above background levels in both enhancing and non-enhancing regions of patients to whom it was administered prior to microdialysis. Future analyses will require paired plasma samples and standards to quantify the expectedly-much higher levels in plasma than brain.

Highest microdialysate levels of caffeine, acetaminophen, and their respective metabolites, at variable peak areas, were found in patients administered these drugs intraoperatively. Caffeine was administered to help NPO patients, having otherwise missed their daily coffee, participate in awake language and neuro-cognitive tasks during eloquent tumor resections. Caffeine has a plasma half-life of 8 hours. Varying baseline levels of caffeine could reflect intake prior to hospitalization. To our knowledge, no prior study has evaluated any of these drugs in human brain or tumor microdialysate. Given their common administration in neurosurgical procedures, further pharmacokinetic characterization may empower their use as reference standards for early phase window-of-opportunity studies evaluating other novel drugs.

Neurosurgical phase 0 studies typically evaluate tissue levels of a single drug, but combination therapies may be needed. Our data suggest feasible analysis of extracellular free drug levels across multiple dialyzable drugs simultaneously in multiple locations. Although we assessed only a single timepoint, dedicated pharmacokinetic microdialysis studies typically quantify drug levels across multiple days. Combining longitudinal pharmacokinetic and metabolomic analyses may reveal candidate pharmacodynamic biomarkers to discern target engagement, therapeutic impact, and markers of early therapeutic resistance.

Technical Variables

Technical details can be paramount to the success of new translational protocols. Given the short intraoperative time window for sampling, we obtained an investigational device exemption to utilize 100 kDA (HMW) catheters and a variable rate microdialysis pump (M Dialysis 107 set to 2µ/min) to help minimize resistance to diffusion and maximize analyte recovery which is often limited by tissue resistance when sampling *in vivo.* Closely related, 20 kDA catheters and the 106 (0.3µL/min) pump are more widely used for pharmacokinetic studies performed over multiple days, and recently enabled pharmacodynamic analyses of cisplatin delivered by reverse microdialysis (*15*). Availability of a 40µL aliquot from each catheter (20 and 40 minutes after catheter placement) allowed both targeted and untargeted analysis of each sample for independent confirmation of 2-HG levels. A caveat is that relative levels of recovery may vary based on catheter. This may merit further consideration in future studies aimed at more precisely examining certain metabolites rather than the global metabolome. HMW catheters can also recover larger analytes including cytokines but are subject to net fluid flux across the membrane. In absence of 2 pumps to keep inflow and outflow equal, oncotic agents such as dextran are utilized to counter net fluid flux. For most patients, our microdialysis solution comprised lactated ringers with 3% dextran 40. Microdialysis for $GBM^{WT}2$ utilized M dialysis' newer brain perfusion fluid with 3% dextran 500. Blank samples of each perfusion fluid recovered from the catheter priming flush prior to microdialysis revealed a different background analyte profile for each (supplemental data). Average lactate levels in samples utilizing LR perfusate were only 14.6% lower than perfusate blanks, and >6x higher than samples obtained from LR-free perfusate highlighting incomplete equilibration achieved across even a 100kDA membrane perfused at 2µL/min. Equilibration and thus analyte recovery can be variably impacted by technical factors including air bubbles within the catheter. Addition of a stable isotope standards in perfusion fluid for key analytes may enable more precise quantification of

brain extracellular levels. Conversely, systemic administration of stable isotope substrates for select metabolic pathways can inform metabolic pathway utilization.

Conclusion: toward individualized metabolic insights

In conclusion, we have shown that acute intraoperative microdialysis for tumor metabolomics is feasible and allows for previously unleveraged access to each patient's diverse tumor extracellular metabolome. This strategy simultaneously yielded analytes correlating separately with IDH status, metabolic phenotype, tumor region and pharmacological agents administered during surgery. Further work in larger cohorts will be needed to elucidate the full array of metabolic signatures observable within and between gliomas and their multi-omic correlates. Specific studies comparing tumor to adjacent brain across multiple tumor subtypes yield an individualized framework for data analysis wherein each patient may serve as their own control to evaluate pharmacodynamic responses to novel, individualized, and combination therapies. The current data derive from 5 unique patients, each of whom has yet to demonstrate further disease progression. These patients and their providers know that future recurrence is inevitable. We present the raw data for these five patients as a first installment toward what we intend to be a growing collaborative, open-source repository of individualized data, in the hopes that such insights can help spur progress to improve otherwise grim prognoses.

MATERIALS AND METHODS

Patient Cohort and Study Design

All study procedures were approved by the Mayo Clinic IRB. Patients provided written informed consent to participate in NCT04047264--an ongoing single group open label single institution study evaluating the safety and feasibility of intraoperative microdialysis. Study eligibility includes adults (>18yo) with known or suspected glioma undergoing tumor resection or biopsy. To date, all enrolled patients have undergone tumor resection. All patients with available analyzed microdialysate samples as of 4/1/2021 (n=5 patients; 15 catheters) were included in the analysis. No patients nor catheters were excluded.

Intraoperative Microdialysis

Each patient underwent intraoperative microdialysis using three M-dialysis 100kDA catheters and 107 variable rate microdialysis pumps under an investigational device exemption. Full details regarding patients, catheters and perfusate are available in supplemental material.

Briefly, catheters were continuously perfused at 2µL/min with isotonic perfusate containing 3% Dextran to balance oncotic pressure and maintain net fluid flux across the catheter membrane. Catheter target locations were selected by the surgeon to facilitate sampling of radiographically diverse regions. The intended catheter depth marked on the catheter with sterile adhesive tape (Steri-Strip). After dural opening but prior to tumor resection, a small pial opening was made at the intended catheter entry sites. The pre-primed catheters were then advanced manually along their planned trajectories to the intended depths with the aid of computer-guided neuronavigation. Cortical surface mapping procedures were performed after catheter implantation, and surgical resection then began, working initially away from the implanted catheters. Throughout this time, collection vials were changed after all catheters were in place, and every 20 minutes thereafter to obtain multiple 40uL aliquots per catheter. Collection continued until at least 2 aliquots had been collected. Each aliquot was immediately labeled and placed directly on dry ice in the operating room. The second aliquot was submitted for metabolomic analysis to minimize potential confounders of variably equilibrated microdialysate in the first aliquot. Any additional aliquots, when available, were saved for future analysis. Catheters were removed prior to resection of the sampled region of brain or tumor. When possible, tissue samples approximately representative of the microdialysis-sampled regions were collected as separate specimens for pathology. When available, CSF was sampled from within the surgical field. With exception of intraoperative microdialysis, no other aspects of the surgical procedure, or post-operative care were altered. Extent of resection was guided in 4 cases by awake language and/or motor mapping as well as intraoperative imaging via computer-guided neuronavigation. 5-ALA fluorescence was additionally used to guide resection of enhancing lesions; intraoperative ultrasound was used to guide extent of non-enhancing lesions. After surgery, microdialysate aliquots were stored at -80C until analyzed. Correlative clinical information including medication timing and dose were obtained from the medical record. No complications occurred that were attributable to use of intraoperative microdialysis. One patient with a large recurrent tumor had expected temporary post-operative exacerbation of baseline hemiparesis. One patient underwent a second surgery 6 months after the index operation for resection of a recurrent growing enhancing lesion though pathology demonstrated only pseudoprogression. As of manuscript submission, all patients remain alive without evidence of tumor recurrence.

Pathology and Molecular Tumor analysis

Tumor samples from each patient underwent standard histopathological analysis for diagnostic purposes. Immunohistochemical analysis for IDH R132H was used to determine IDH status. Negative cases were confirmed by IDH1/2 sequencing. GBMs were evaluated for MGMT methylation. TERT promotor mutations were identified by sequencing. 1p/19q co-deletion, CDKN2A status and karyotype complexity were evaluated via chromosomal microarray.

Targeted Analysis of D/L2-HG

Targeted metabolomic analysis of microdialysate and CSF samples was performed by the Mayo Clinic metabolomic core facility. L and D isomers of 2-hydroxyglutaratic acid were separated and quantified by liquid chromatography mass spectrometry (LC/MS) using slight modifications to previously described methods(*25-27*). Briefly, internal standard solution containing U-13C labeled 2-hydroxyglutarate was added to microdialysate. Proteins were removed by adding 500µl of chilled 80% methanol solution to the sample mixture. The mixture was allowed to incubate on ice for 40 minutes prior to removal of the supernatant. After drying the supernatant in the speed vac under medium heat, the samples were derivatized with Diacetyl-L-Tartaric Anhydride (25 mg/ml in 4:1 dichloromethane: acetic acid). Samples were dried and resuspended in 100µL of water before analysis on a Nexera X2 UPLC module coupled with an AB Sciex Triple Quad 6500 mass spectrometer. Metabolites were separated on an Acquity HSS-T3, 1.8 µm, 2.1 x 50 mm column (Waters Corp, MA, USA), held at 40 °C, using 99% water, 1% acetonitrile, and 5 mM ammonium formate in water, adjusted to pH 3.3 with formic acid, as mobile phase A and 99%acetonitrile, 1% water, and 0.1% formic acid as mobile phase B. The flow rate was 0.3 mL/min and 2-HG D- and L- isomers were separated with an isocratic elution (99%A, 1%B) for 8 minutes. The mass spectrometer was operated in ESI-mode, monitoring mass transitions of m/z 363 -› 147 for DATAN labeled 2-HG and 147 -› 129 for 2-HG. Concentrations of both isomers were measured against a 10-point calibration curves that underwent the same derivatization. Using these methods, we have established a limit of quantification of 20nM, with an inter-sample coefficient of variance of 11.30%. Human bone marrow plasma as a biological reference contains 0.52µM D2-HG.

Untargeted Metabolomic Analysis

Untargeted metabolomic analysis of the microdialysate was performed by Metabolon, Inc. Seventeen microdialysate samples were analyzed: 2 blanks comprised perfusate that had passed through catheters C of patients O^{III} and $GBM^{WT}2$ during the flush cycle prior to collecting the first aliquot. Fifteen microdialysate samples comprised the 2nd aliquot collected from each

catheter (3 catheters in 15 patients) after intraoperative placement within the tissue. Following a step intended for protein removal, four fractions of the metabolite extract were randomly run across the platform and analyzed by ultra-performance liquid chromatography tandem mass spectrometry (UPLC-MS/MS) which combines physical separation of liquid chromatography with the mass analysis capabilities of mass spectrometry. Two fractions were evaluated with reverse phase (RP) UPLC-MS/MS with positive ion mode ESI, one by RP/UPLC-MS/MS with negative ion mode ESI, and one with Hydrophobic interaction chromatography (HILIC) UPLC-MS/MS with negative ion mode ESI. Throughout the sample processing, multiple controls were analyzed with the experimental samples, including a pooled matrix sample, extracted water samples, and a cocktail of QC standards for instrument performance monitoring and chromatographic alignment. Relative standard deviation was measured for instrument variability control and overall process variability was determined by median relative standard deviation (RSD) for all endogenous metabolites. Raw data was extracted from UPLC-MS/MS results, peak-identified, and QC processed according to Metabolon standards. Metabolites were identified by compared data to Metabolon's library which includes information on retention index (RI), mass to charge ratio (m/z), and chromatographic data of molecules. One sample ($GBM^{WT}1$: Catheter B) was found by Metabolon to contain <20µL, and samples were run with a 50% dilution. As such, identified peak areas for metabolites in this sample were doubled prior to use in analysis. Otherwise, raw values for area under the curve were used for relative quantitative analysis.

Of the 353 biochemicals detected in the microdialysate samples, 315 were assigned a named chemical identity by metabolon; 181 of these were detected in all 15 samples and thus used for clustering, correlation, and enrichment analyses. Full raw data are provided in supplemental materials.

Statistical Analysis

Data are presented as peak areas from Metabolon, where applicable, and are available in Supplemental File 1. MetaboAnalyst 5.0 was used for hierarchical clustering heat maps, machine learning algorithms (PCA, PLS-DA, sPLS-DA, OPLS-DA), and FC analyses. Data from Metabolon underwent generalized logarithmic transformation, with no normalization, in MetaboAnalyst. Enrichment Analysis was performed using GSEA 4.1.0 (Gene set enrichment) repurposed for metabolite set analysis using custom feature sets. Graphs were generated using GraphPad PRISM 9.1. FDR <0.05 was considered statistically significant for enrichment

analysis; P<0.05 and FC>2 was considered significant for FC analysis. Further details of statistical analysis workflows are provided below.

MetaboAnalyst

Metabolomic analyses were performed using MetaboAnalyst, a publicly available, web-based tool to analyze and visualize metabolomic data (*28*). The peak area data for the 181 metabolites present across all 15 samples was input into MetaboAnalyst. To limit manipulation of the samples, samples were transformed by a generalized logarithmic transformation in all analyses without filtering.

Supervised and Unsupervised Metabolomic Analyses

Catheter samples were subdivided into groups based on variables including IDH-status, pathology (glioblastoma vs oligodendroglioma), patient identity, and tumor versus brain, as well as empirically identified metabolic phenotype (α and β Table 2). Brain samples were excluded to enable comparisons between tumor subtypes. Analyses based on IDH status and brain vs tumor were planned *a priori*. Other analyses were performed post-hoc. Given the desire to elucidate individualized n=1 tumor signatures by comparing catheters within individual patients, each catheter was analyzed as a unique sample with clustering analyses used to determine the relative importance of each variable. To optimize transparency and mitigate the risk of data overinterpretation, group-wise comparisons were subject to multiple statistical and clustering analyses. To ensure conservative analysis with minimal risk of introduced bias, comparisons were based on the full cohort of 181 metabolites quantifiable in all 15 microdialysis samples. No metabolites were filtered or excluded; no data interpolation steps were performed.

To evaluate apparent groupings within the data in an unbiased manner, we started with Principal Component Analysis (PCA)--an unsupervised machine learning algorithm that reduces the dimensionality of large data sets to highlight the most prominent patterns in a data set (*29*). Following this, supervised machine learning algorithms were utilized based on candidate groupings, including Partial Least Squares-Discriminant Analysis (PLS-DA), which guides the group analysis by accounting for the group nomenclature provided to the machine learning algorithm (*30*). Sparse PLS-DA (sPLS-DA) was also performed, which selects the most predictive variables between various groups (*31*). Finally, orthogonal projection to latent structures – DA (OPLS-DA) adds orthogonal signal correction to PLS-DA (*32*). Clustering of groups was evaluated using each of these machine learning algorithms.

Pearson Correlation, Hierarchical Clustering Heat Maps, and Volcano Plots

Pearson Correlation maps were generated in Metaboanalyst based on features (metabolites present across all samples) and samples. Heat maps were generated using the hierarchical clustering heat map package on MetaboAnalyst from the glog (generalized logarithm) transformed data. Heat maps utilized the Euclidean distance between points; Ward's method was used for clustering analysis to minimize within-cluster variance. Heat maps were generated for the top 25 or top 50 group-associated metabolites based on t-test/ANOVA values, as specified in the results. Volcano plots were generated using a fold change threshold of 2.0 and p-value threshold of 0.05 with equal group variance for significance.

Enrichment Analysis

Analysis of samples from individual patients may generate insufficient power to draw conclusions based on any single metabolite. However, untargeted metabolomic analysis of even two catheters can yield a ranked list of differentially abundant metabolites in one catheter versus the other. Gene Set Enrichment Analysis (GSEA) is the most widely utilized analytical method for rank-based analysis of data sets in biomedicine, developed for comparing gene expression data sets. Although a metabolite set enrichment analysis is available in MetaboAnalyst, GSEA provided generally more conservative enrichment estimates and provided more granular visualization and analytical tools to help identify the most important metabolites driving enrichment. GSEA is frequently performed using curated gene sets from the molecular signatures database (MSigDB), though custom feature sets can be used enabling enrichment analysis of metabolites rather than metabolites. We created ranked metabolite lists for each of our 15 catheter samples by comparing them to other catheter samples for that same patient. The lists were ranked based on fold change. We also created over 350 metabolite libraries against which these ranked lists could be compared to determine relative positive and negative enrichment (supplemental data, .gmx file). These libraries were generated based on fold change, t-test values, and signal-to-noise ratio of both human and mouse metabolomic data from prior and ongoing studies. Additionally, results from previously published papers(*14, 15, 33-35*), and KEGG-based metabolite sets were included for external reference. The number of feature sets evaluated is included in calculations to generate a normalized enrichment score and FDR for each.

The full ranked metabolite lists (.rnk) of catheter A vs C for patients with both enhancing tumor and brain (n=3) were used as the reference data against which to assess relative enrichment using the custom .gmx file. This .gmx file included the top 75 metabolites comparing catheters A (enhancing) versus C (brain) for each patient with GBM (GBM^{mut}, GBM^{WT}A, and

GBM^{WT}B) As such, 6 analyses were enabled to evaluate enrichment for the top A versus C metabolites (enriched in enhancing tumor versus brain) from each patient in each other patient. The same was performed for C versus A to identify metabolites reproducibly enriched in brain relative to enhancing tumor. From here, we noted how often each metabolite was present in the leading edge of enrichment for each analysis with the maximum being 6 out 6. Metabolites were only listed if they were present in the "leading edge" of enrichment for at least 4/6 analyses ensuring each patient was included in at least one comparison. Those in the leading edge of 6/6 analyses were listed in bold (Fig 3D, E).

Acknowledgements: We would like to thank all of our patients who selflessly participated in this study, without whom this work and any advancement in the field of neuro-oncology would truly not be possible.

References

1. R. Stupp *et al.*, Radiotherapy plus concomitant and adjuvant temozolomide for glioblastoma. *N Engl J Med* **352**, 987-996 (2005).
2. H. Yan *et al.*, IDH1 and IDH2 mutations in gliomas. *N Engl J Med* **360**, 765-773 (2009).
3. Q. SongTao *et al.*, IDH mutations predict longer survival and response to temozolomide in secondary glioblastoma. *Cancer Sci* **103**, 269-273 (2012).
4. S. Shibao *et al.*, Metabolic heterogeneity and plasticity of glioma stem cells in a mouse glioblastoma model. *Neuro Oncol* **20**, 343-354 (2018).
5. Y. Kondo, K. Katsushima, F. Ohka, A. Natsume, K. Shinjo, Epigenetic dysregulation in glioma. *Cancer Sci* **105**, 363-369 (2014).
6. A. Kathagen-Buhmann *et al.*, Glycolysis and the pentose phosphate pathway are differentially associated with the dichotomous regulation of glioblastoma cell migration versus proliferation. *Neuro Oncol* **18**, 1219-1229 (2016).
7. E. Vlashi *et al.*, Metabolic state of glioma stem cells and nontumorigenic cells. *Proc Natl Acad Sci U S A* **108**, 16062-16067 (2011).
8. M. Strickland, E. A. Stoll, Metabolic Reprogramming in Glioma. *Front Cell Dev Biol* **5**, 43 (2017).
9. J. Lynes *et al.*, Cytokine Microdialysis for Real-Time Immune Monitoring in Glioblastoma Patients Undergoing Checkpoint Blockade. *Neurosurgery* **84**, 945-953 (2019).
10. J. Portnow *et al.*, A pilot microdialysis study in brain tumor patients to assess changes in intracerebral cytokine levels after craniotomy and in response to treatment with a targeted anti-cancer agent. *J Neurooncol* **118**, 169-177 (2014).

11. J. O. Blakeley *et al.*, Effect of blood brain barrier permeability in recurrent high grade gliomas on the intratumoral pharmacokinetics of methotrexate: a microdialysis study. *J Neurooncol* **91**, 51-58 (2009).
12. C. Joukhadar, M. Müller, Microdialysis: current applications in clinical pharmacokinetic studies and its potential role in the future. *Clin Pharmacokinet* **44**, 895-913 (2005).
13. J. Ryals, K. Lawton, D. Stevens, M. Milburn, Metabolon, Inc. (2007).
14. C. Wibom *et al.*, Metabolomic patterns in glioblastoma and changes during radiotherapy: a clinical microdialysis study. *J Proteome Res* **9**, 2909-2919 (2010).
15. B. Bjorkblom *et al.*, Metabolic response patterns in brain microdialysis fluids and serum during interstitial cisplatin treatment of high-grade glioma. *Br J Cancer* **122**, 221-232 (2020).
16. J. L. Markley *et al.*, The future of NMR-based metabolomics. *Curr Opin Biotechnol* **43**, 34-40 (2017).
17. N. Xiong *et al.*, Using arterial-venous analysis to characterize cancer metabolic consumption in patients. *Nat Commun* **11**, 3169 (2020).
18. S. Han *et al.*, IDH mutation in glioma: molecular mechanisms and potential therapeutic targets. *Br J Cancer* **122**, 1580-1589 (2020).
19. K. Tateishi *et al.*, Extreme Vulnerability of IDH1 Mutant Cancers to NAD+ Depletion. *Cancer Cell* **28**, 773-784 (2015).
20. A. Linninger *et al.*, Modeling the diffusion of D-2-hydroxyglutarate from IDH1 mutant gliomas in the central nervous system. *Neuro Oncol* **20**, 1197-1206 (2018).
21. Z. Konteatis *et al.*, Vorasidenib (AG-881): A First-in-Class, Brain-Penetrant Dual Inhibitor of Mutant IDH1 and 2 for Treatment of Glioma. *ACS Med Chem Lett* **11**, 101-107 (2020).
22. A. R. Molloy *et al.*, MR-detectable metabolic biomarkers of response to mutant IDH inhibition in low-grade glioma. *Theranostics* **10**, 8757-8770 (2020).
23. O. C. Andronesi *et al.*, Pharmacodynamics of mutant-IDH1 inhibitors in glioma patients probed by in vivo 3D MRS imaging of 2-hydroxyglutarate. *Nat Commun* **9**, 1474 (2018).
24. K. J. Wenger *et al.*, Non-Invasive Measurement of Drug and 2-HG Signals Using (19)F and (1)H MR Spectroscopy in Brain Tumors Treated with the Mutant IDH1 Inhibitor BAY1436032. *Cancers (Basel)* **12**, (2020).
25. W. M. Oldham, J. Loscalzo, Quantification of 2-Hydroxyglutarate Enantiomers by Liquid Chromatography-mass Spectrometry. *Bio Protoc* **6**, (2016).
26. E. A. Struys, E. E. Jansen, N. M. Verhoeven, C. Jakobs, Measurement of urinary D- and L-2-hydroxyglutarate enantiomers by stable-isotope-dilution liquid chromatography-tandem mass spectrometry after derivatization with diacetyl-L-tartaric anhydride. *Clin Chem* **50**, 1391-1395 (2004).
27. Q. Y. Cheng *et al.*, Sensitive Determination of Onco-metabolites of D- and L-2-hydroxyglutarate Enantiomers by Chiral Derivatization Combined with Liquid Chromatography/Mass Spectrometry Analysis. *Sci Rep* **5**, 15217 (2015).
28. Z. Pang *et al.*, MetaboAnalyst 5.0: narrowing the gap between raw spectra and functional insights. *Nucleic Acids Res* **49**, W388-w396 (2021).
29. S. Wold, K. Esbensen, P. Geladi, Principal component analysis. *Chemometrics and intelligent laboratory systems* **2**, 37-52 (1987).

30. R. G. Brereton, G. R. Lloyd, Partial least squares discriminant analysis: taking the magic away. *Journal of Chemometrics* **28**, 213-225 (2014).
31. D. Chung, S. Keles, Sparse partial least squares classification for high dimensional data. *Stat Appl Genet Mol Biol* **9**, Article17 (2010).
32. M. Bylesjö *et al.*, OPLS discriminant analysis: combining the strengths of PLS-DA and SIMCA classification. *Journal of Chemometrics: A Journal of the Chemometrics Society* **20**, 341-351 (2006).
33. T. C. Glenn *et al.*, Metabolomic analysis of cerebral spinal fluid from patients with severe brain injury. *Acta Neurochir Suppl* **118**, 115-119 (2013).
34. M. Eiden *et al.*, Discovery and validation of temporal patterns involved in human brain ketometabolism in cerebral microdialysis fluids of traumatic brain injury patients. *EBioMedicine* **44**, 607-617 (2019).
35. J. Huang *et al.*, A prospective study of serum metabolites and glioma risk. *Oncotarget* **8**, 70366-70377 (2017).

Figure 1

A

Patient ID	Pathology	IDH Status	Other molecular/genetic features	Catheter A	Catheter B	Catheter C
O^{II}	**Oligodendroglioma** WHO II	**Mutant**	1p/19q co-deletion; TERT-mutant	FLAIR	FLAIR	FLAIR
O^{III}	**Oligodendroglioma** WHO III	**Mutant**	1p/19q co-deletion; TERT-mutant	FLAIR	FLAIR	FLAIR
GBM^{mut}	**Glioblastoma** (Recurrent)	**Mutant**	MGMT non-methylated; loss of CDKN2A/B; complex karyotype	Enhancing	FLAIR	Brain
$GBM^{WT}1$	**Glioblastoma**	**Wild-type**	MGMT non-methylated; loss of CDKN2A/B	Enhancing	FLAIR	Brain
$GBM^{WT}2$	**Glioblastoma**	**Wild-type**	Indeterminate MGMT methylation*	Enhancing	FLAIR	Brain

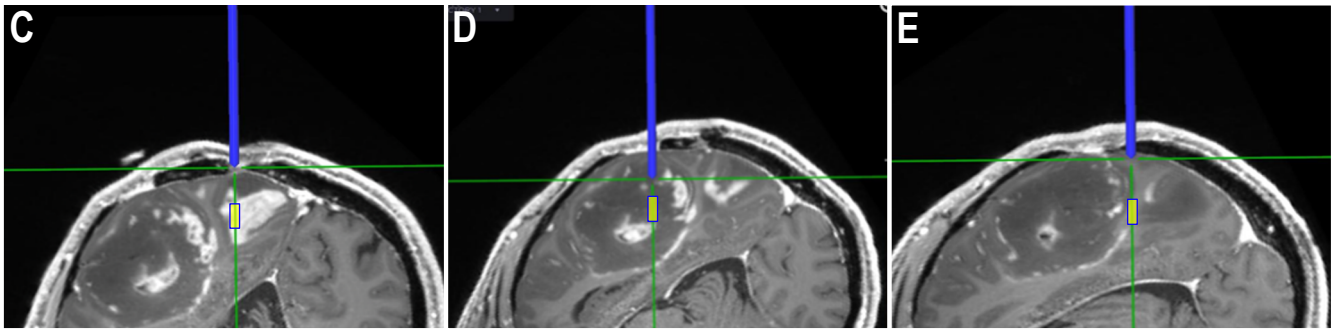

Catheter A **Catheter B** **Catheter C**

Figure 2

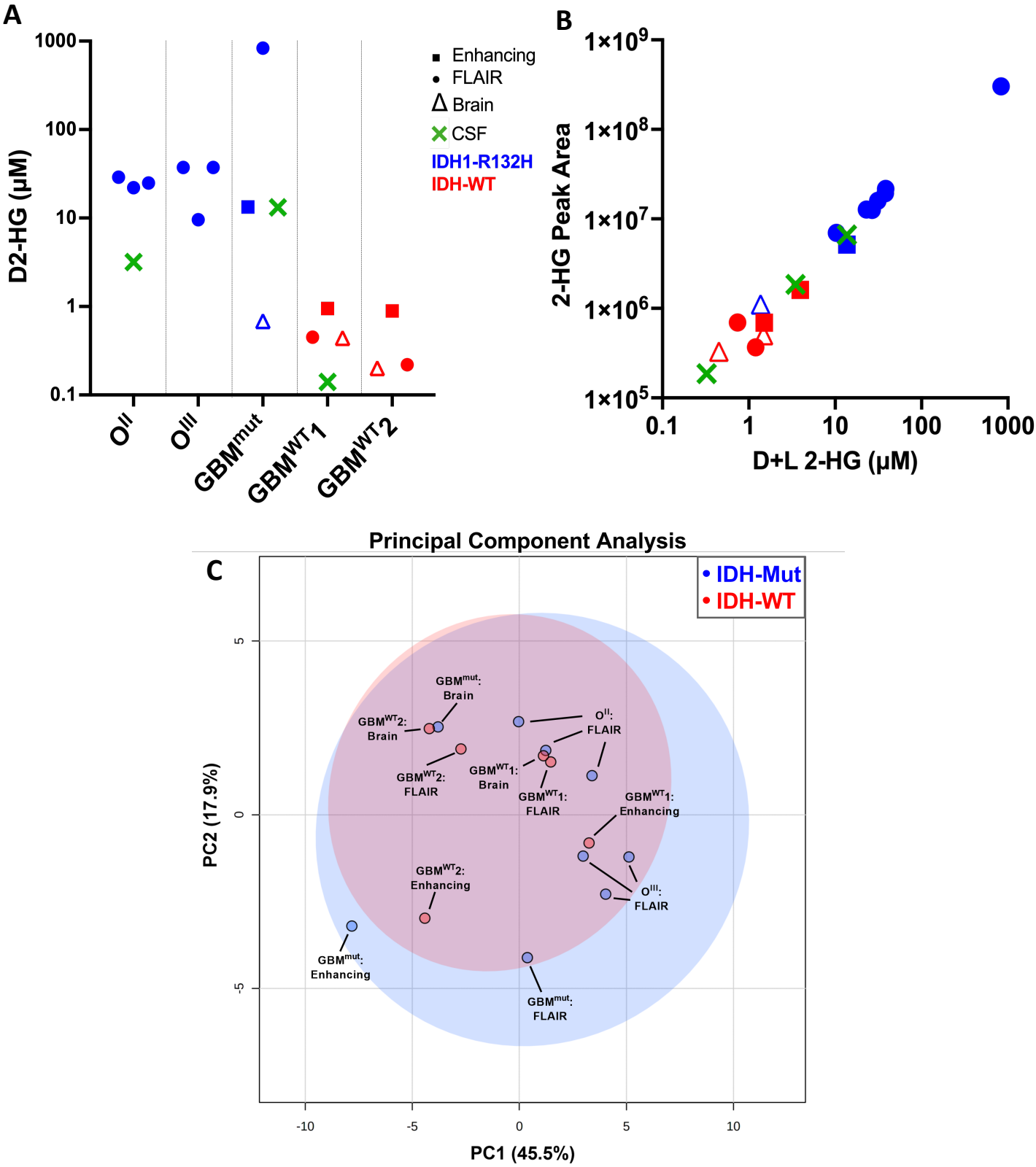
A
D2-HG (μM)
1000
100
10
1
0.1
Enhancing
FLAIR
Brain
CSF
IDH1-R132H
IDH-WT
O^II
O^III
GBM^mut
GBM^WT1
GBM^WT2
B
2-HG Peak Area
1×10^9
1×10^8
1×10^7
1×10^6
1×10^5
0.1
1
10
100
1000
D+L 2-HG (μM)
Principal Component Analysis
C
IDH-Mut
IDH-WT
PC2 (17.9%)
PC1 (45.5%)
5
0
-5
-10
10
GBM^mut: Brain
GBM^WT2: Brain
O^II: FLAIR
GBM^WT2: FLAIR
GBM^WT1: Brain
GBM^WT1: FLAIR
GBM^WT1: Enhancing
GBM^WT2: Enhancing
O^III: FLAIR
GBM^mut: Enhancing
GBM^mut: FLAIR

A Positive enrichment for GBM^{mut}: A in GBM^{WT}2: A vs. C

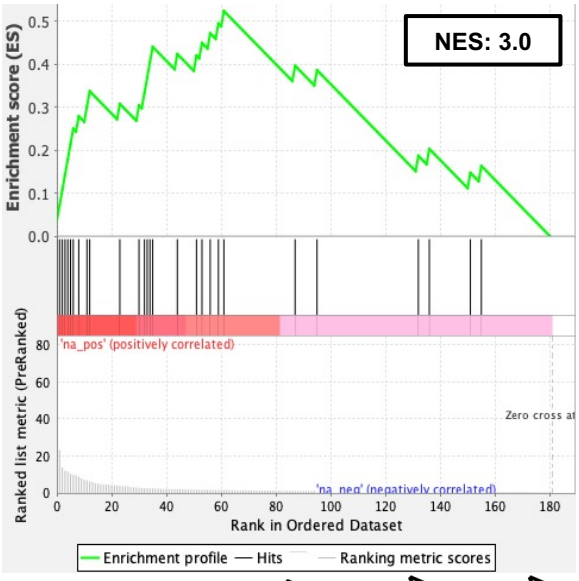

B Negative enrichment for GBM^{mut}: A in GBM^{WT}2: C vs. A

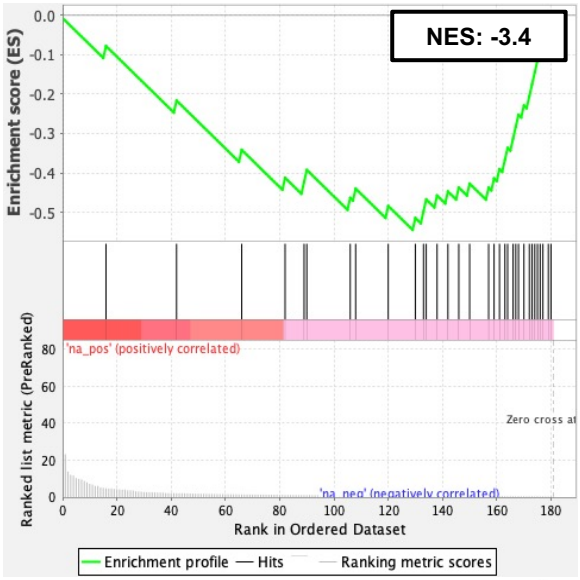

C

	GBM^{mut}: A	GBM^{WT}1: A	GBM^{WT}2: A	FDR GBM^{mut}: A	FDR GBM^{WT}1: A	FDR GBM^{WT}2: A
GBM^{mut}: A (Enhancing)	6.1	4.0	3.8	0.0	0	0
GBM^{WT}1: A (Enhancing)	2.3	5.9	2.2	0.0017	0	0.0076
GBM^{WT}2: A (Enhancing)	3.0	2.8	5.9	0	6.82E-05	0
GBM^{mut}: C (Brain)	-6.2	-2.8	-3.2	0	1.08E-04	0
GBM^{WT}1: C (Brain)	-2.9	-6.0	-3.3	0	0	0
GBM^{WT}2: C (Brain)	-3.4	-3.1	-6.3	0	0	0
Tumor (Björkblom, 2020)	3.7	2.2	2.2	0	0.0031	0.006
Brain (Björkblom, 2020)	-2.2	-1.4	-1.5	0.0076	0.21	0.14
Tumor (Wibom, 2010)	3.0	2.3	2.1	0	0.0024	0.013
TBI Microdialysate	1.8	2.0	1.8	0.034	0.014	0.044
TBI CSF	-0.8	-1.6	-1.2	0.77	0.09	0.40

NES: 5, 0, -5

D

Enhancing Tumor		
3-Methylhistidine	Guanidoacetic acid	N(6)-Methyllysine
L-Proline	L-Tyrosine	L-Valine
2-HG	Alpha-ketoisovaleric acid	Dimethylglycine
Imidazolelactic acid	Ketoleucine	L-Alanine
L-Asparagine	L-Histidine	L-Leucine
L-Tryptophan	2PY	S-Methyl-L-cysteine
Homo-L-Arginine		

E

Brain	
DMTPA	2-O-Methylascorbic acid
Arabinonic acid	D-Arabitol
Erythronic acid	Inosine
L-Aspartic acid	NAAG
N-Acetylneuraminic acid	N-Acetylserine
Ribonic acid	3-Hydroxymethylglutaric acid
Gulonic acid	NAA
N-Acetylglutamine	Phosphate

Figure 4

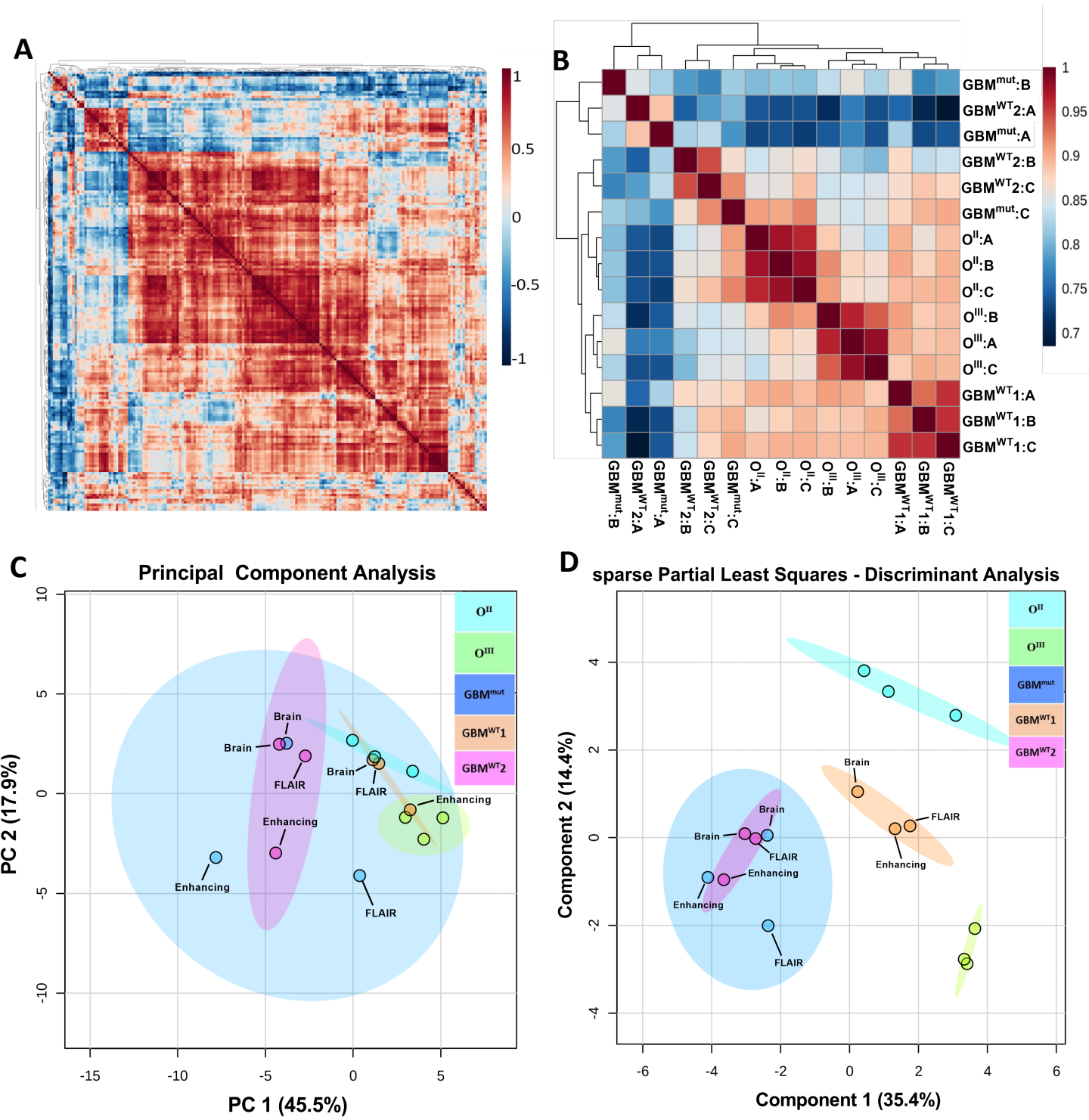
A
1
0.5
0
-0.5
-1
B
GBMmut:B
GBMWT2:A
GBMmut:A
GBMWT2:B
GBMWT2:C
GBMmut:C
OII:A
OII:B
OII:C
OIII:B
OIII:A
OIII:C
GBMWT1:A
GBMWT1:B
GBMWT1:C
1
0.95
0.9
0.85
0.8
0.75
0.7
C
Principal Component Analysis
PC 2 (17.9%)
PC 1 (45.5%)
OII
OIII
GBMmut
GBMWT1
GBMWT2
Brain
FLAIR
Enhancing
D
sparse Partial Least Squares - Discriminant Analysis
Component 2 (14.4%)
Component 1 (35.4%)
OII
OIII
GBMmut
GBMWT1
GBMWT2
Brain
FLAIR
Enhancing

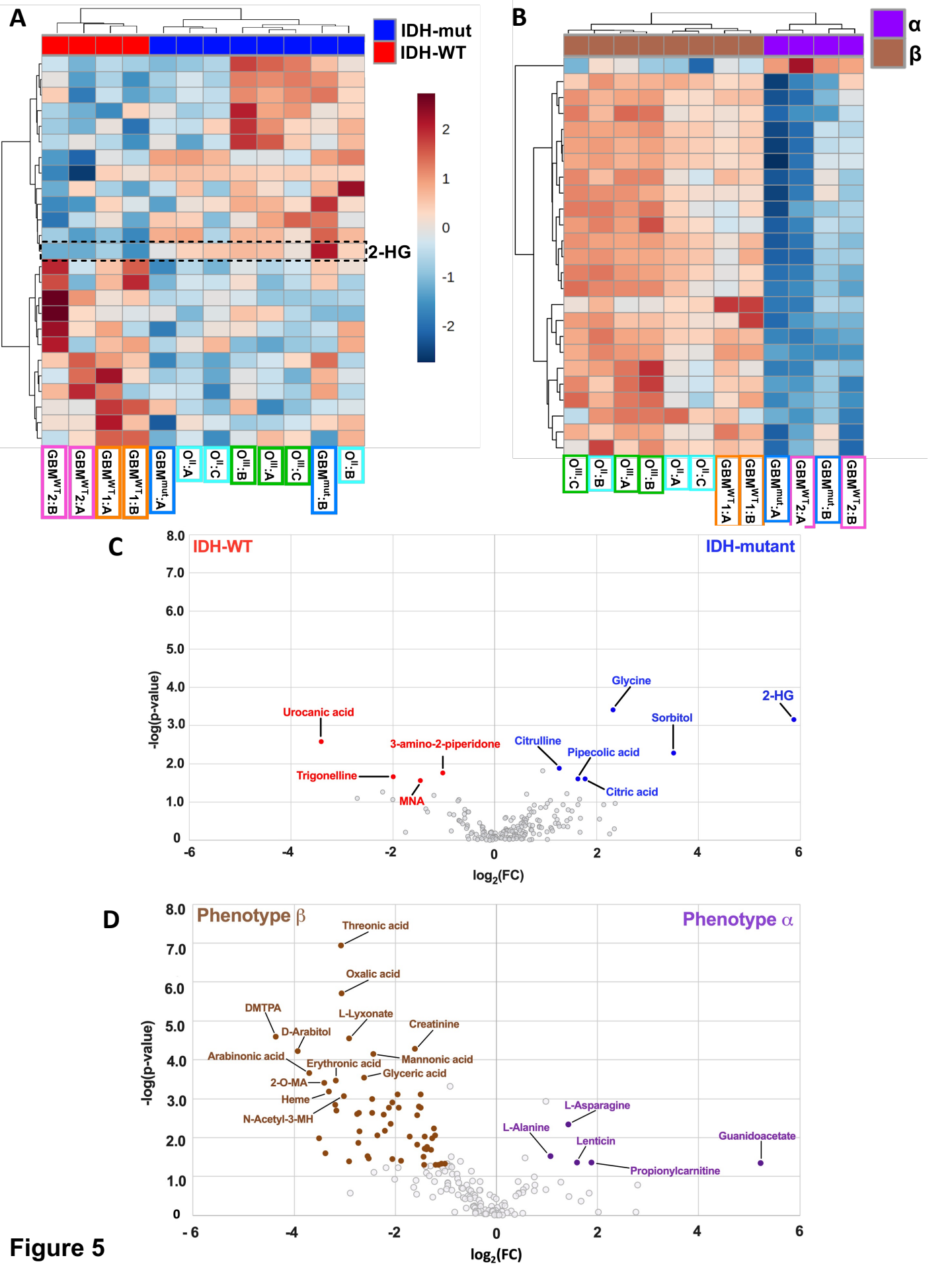
A
IDH-mut
IDH-WT
2-HG
2
1
0
-1
-2
GBM^WT 2:B
GBM^WT 2:A
GBM^WT 1:A
GBM^WT 1:B
GBM^mut.:A
O^II.:A
O^II.:C
O^III.:B
O^III.:A
O^III.:C
GBM^mut.:B
O^II.:B
B
α
β
O^III.:C
O^II.:B
O^III.:A
O^III.:B
O^II.:A
O^II.:C
GBM^WT 1:A
GBM^WT 1:B
GBM^mut.:A
GBM^WT 2:A
GBM^mut.:B
GBM^WT 2:B
C
IDH-WT
IDH-mutant
-log(p-value)
log2(FC)
Urocanic acid
3-amino-2-piperidone
Trigonelline
MNA
Citrulline
Pipecolic acid
Citric acid
Glycine
Sorbitol
2-HG
D
Phenotype β
Phenotype α
Threonic acid
Oxalic acid
DMTPA
D-Arabitol
L-Lyxonate
Creatinine
Arabinonic acid
Erythronic acid
Mannonic acid
Glyceric acid
2-O-MA
Heme
N-Acetyl-3-MH
L-Asparagine
L-Alanine
Lenticin
Guanidoacetate
Propionylcarnitine
-log(p-value)
log2(FC)

Figure 5

Figure 6

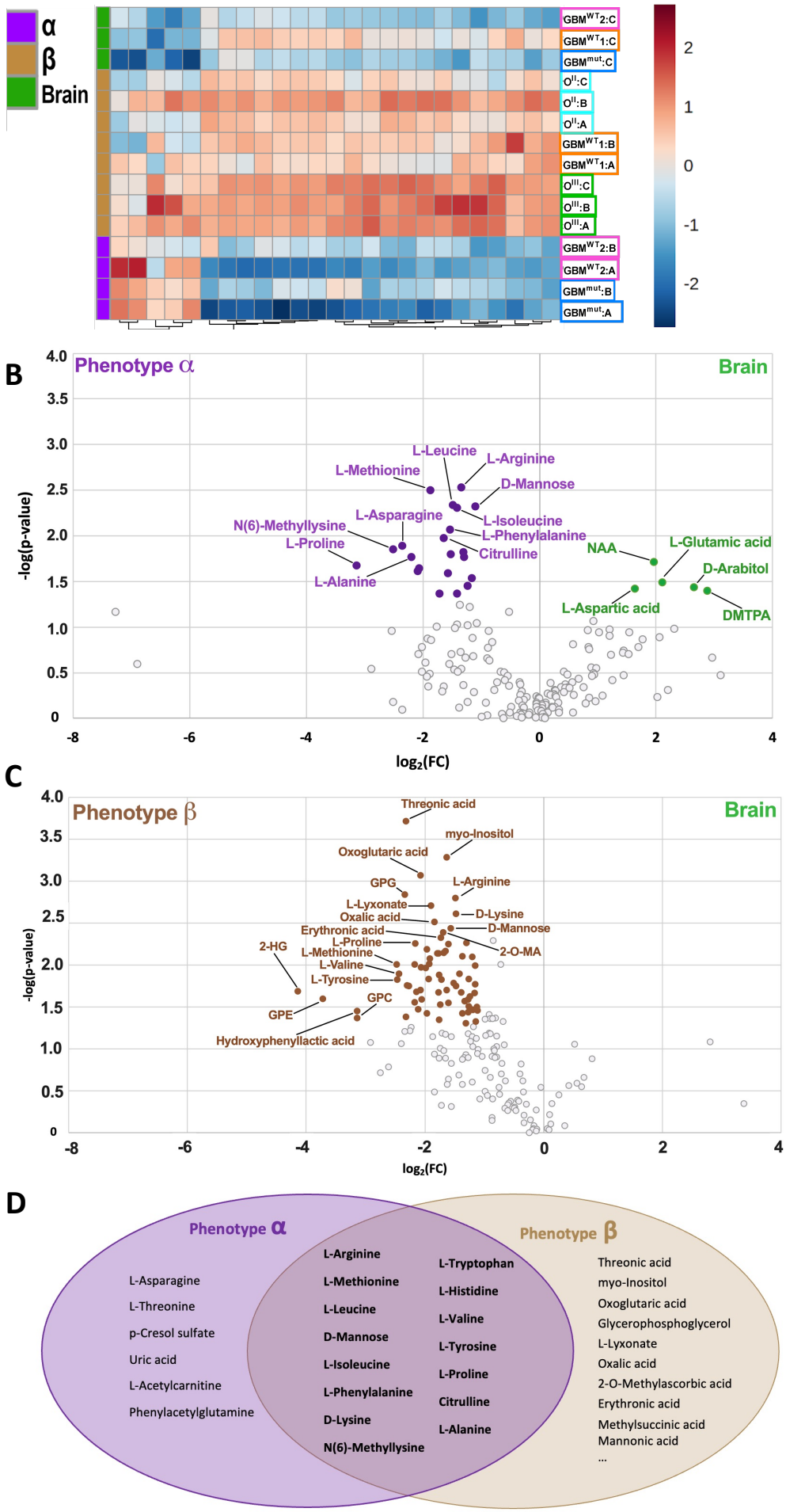
A
α
β
Brain
GBMWT2:C
GBMWT1:C
GBMmut:C
OII:C
OII:B
OII:A
GBMWT1:B
GBMWT1:A
OIII:C
OIII:B
OIII:A
GBMWT2:B
GBMWT2:A
GBMmut:B
GBMmut:A
2
1
0
-1
-2
B
Phenotype α
Brain
-log(p-value)
log2(FC)
L-Leucine
L-Arginine
L-Methionine
D-Mannose
L-Asparagine
L-Isoleucine
N(6)-Methyllysine
L-Phenylalanine
L-Proline
Citrulline
NAA
L-Glutamic acid
D-Arabitol
L-Alanine
L-Aspartic acid
DMTPA
C
Phenotype β
Brain
-log(p-value)
log2(FC)
Threonic acid
myo-Inositol
Oxoglutaric acid
GPG
L-Arginine
L-Lyxonate
D-Lysine
Oxalic acid
Erythronic acid
D-Mannose
L-Proline
2-HG
2-O-MA
L-Methionine
L-Valine
L-Tyrosine
GPC
GPE
Hydroxyphenyllactic acid
D
Phenotype α
Phenotype β
L-Asparagine
L-Threonine
p-Cresol sulfate
Uric acid
L-Acetylcarnitine
Phenylacetylglutamine
L-Arginine
L-Methionine
L-Leucine
D-Mannose
L-Isoleucine
L-Phenylalanine
D-Lysine
N(6)-Methyllysine
L-Tryptophan
L-Histidine
L-Valine
L-Tyrosine
L-Proline
Citrulline
L-Alanine
Threonic acid
myo-Inositol
Oxoglutaric acid
Glycerophosphoglycerol
L-Lyxonate
Oxalic acid
2-O-Methylascorbic acid
Erythronic acid
Methylsuccinic acid
Mannonic acid
...

Figure 7

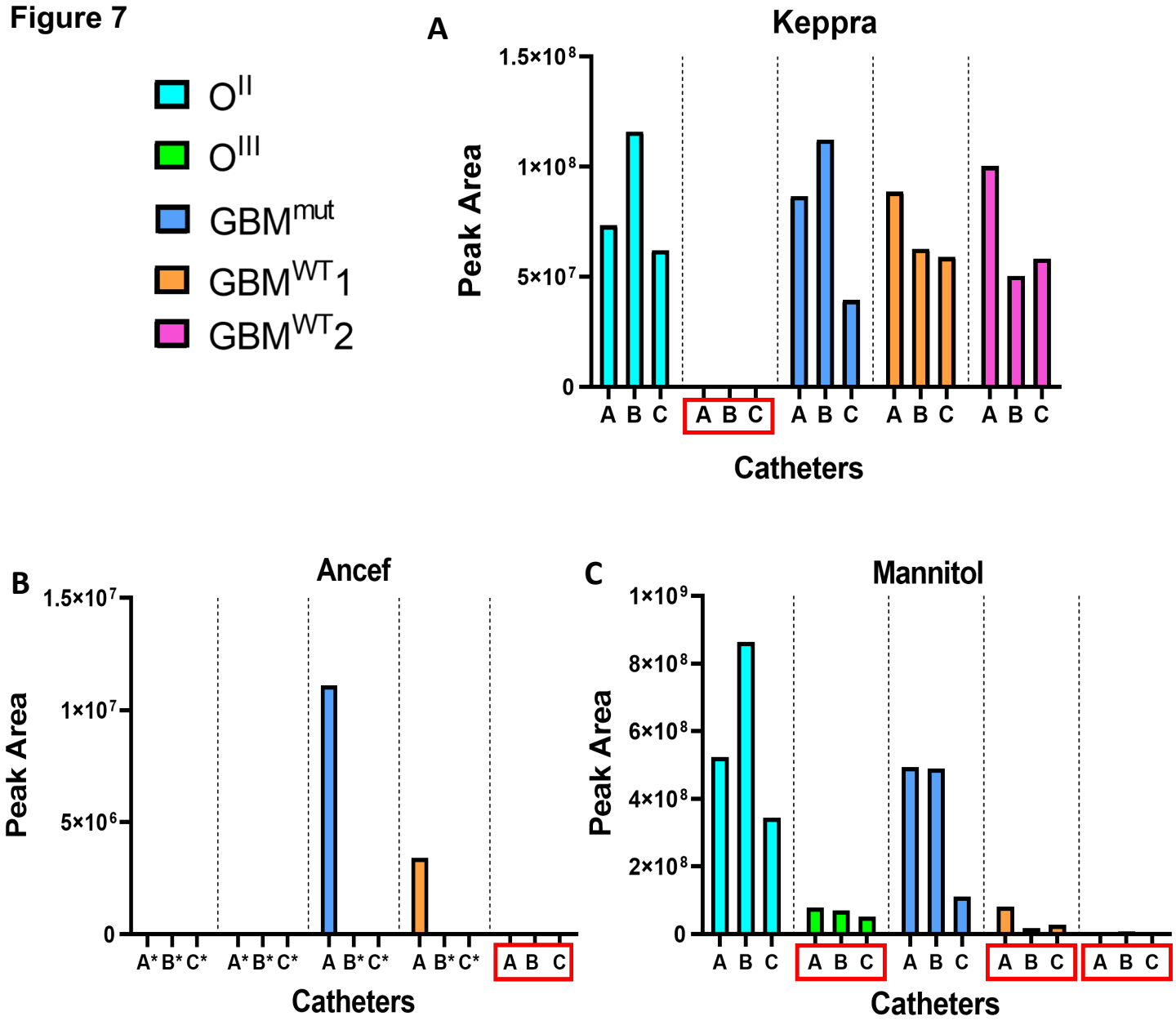
O^II
O^III
GBM^mut
GBM^WT1
GBM^WT2
A
Keppra
Peak Area
1.5×10^8
1×10^8
5×10^7
0
A B C A B C A B C A B C A B C
Catheters
B
Ancef
Peak Area
1.5×10^7
1×10^7
5×10^6
0
A* B* C* A* B* C* A B* C* A B* C* A B C
Catheters
C
Mannitol
Peak Area
1×10^9
8×10^8
6×10^8
4×10^8
2×10^8
0
A B C A B C A B C A B C A B C
Catheters

Supplemental Figure 1

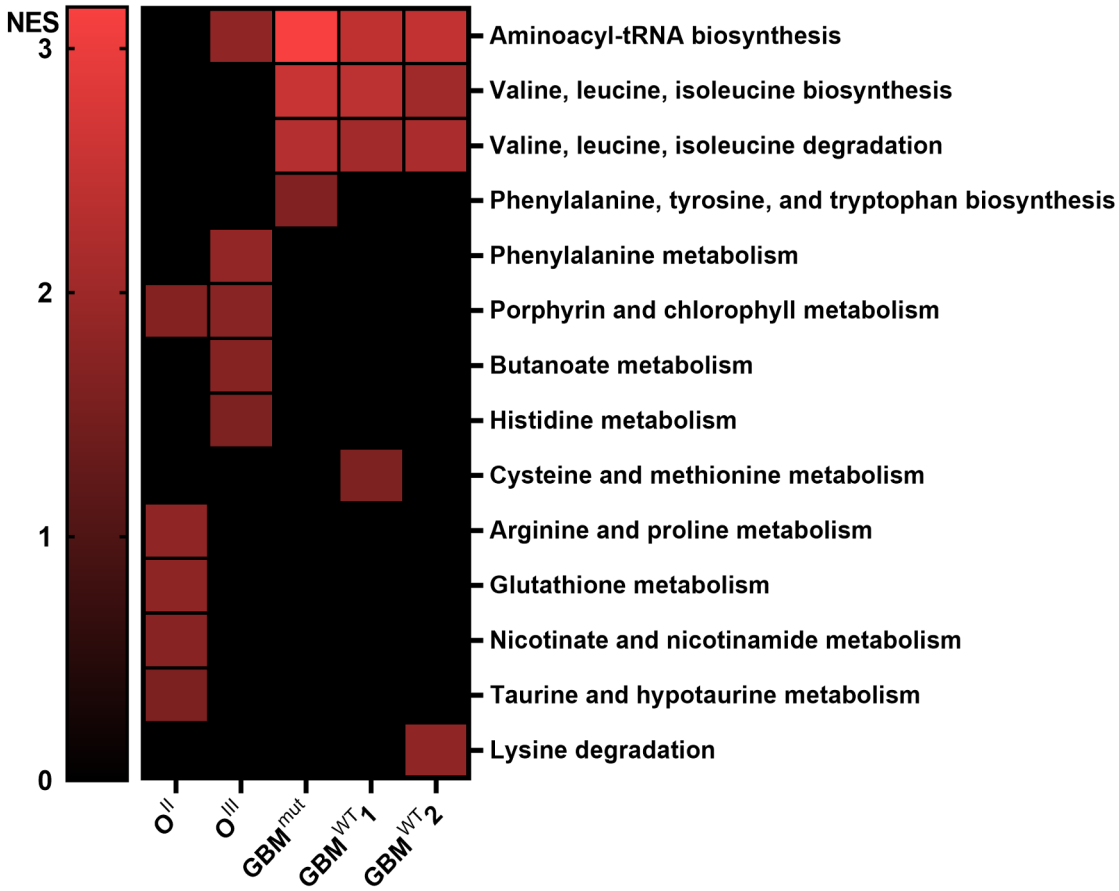

Supplemental Figure 2

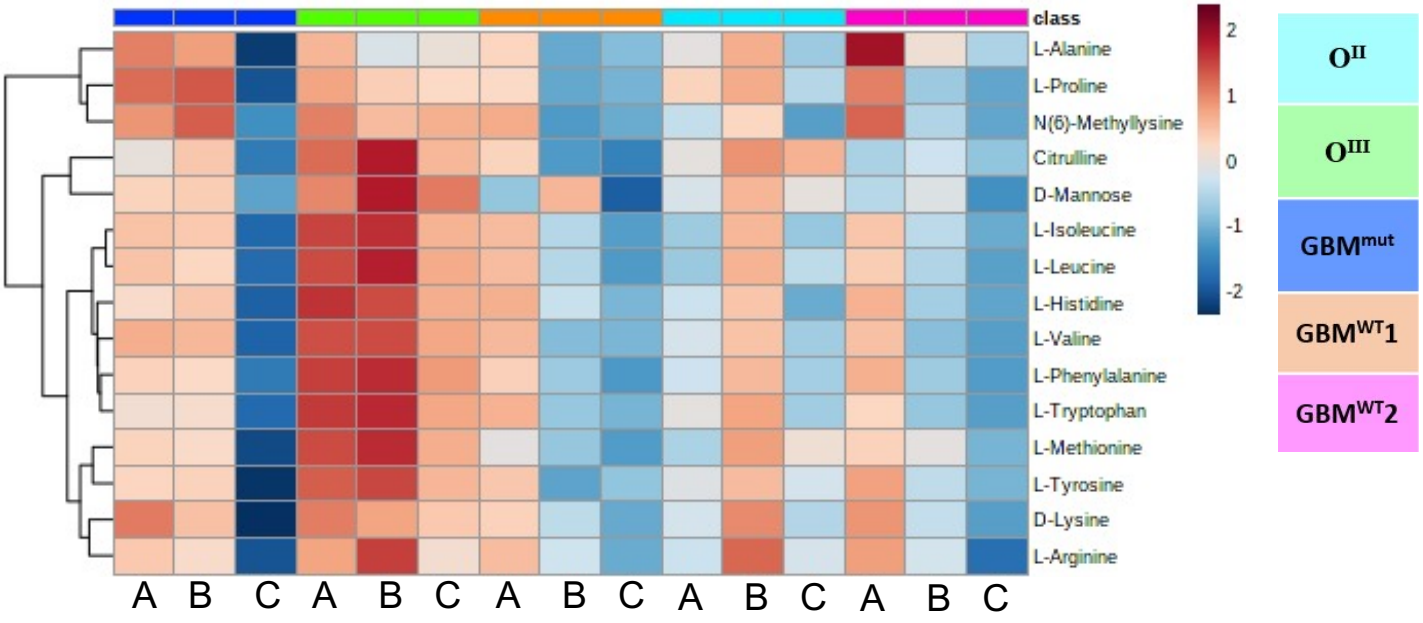

Supplemental Figure 3

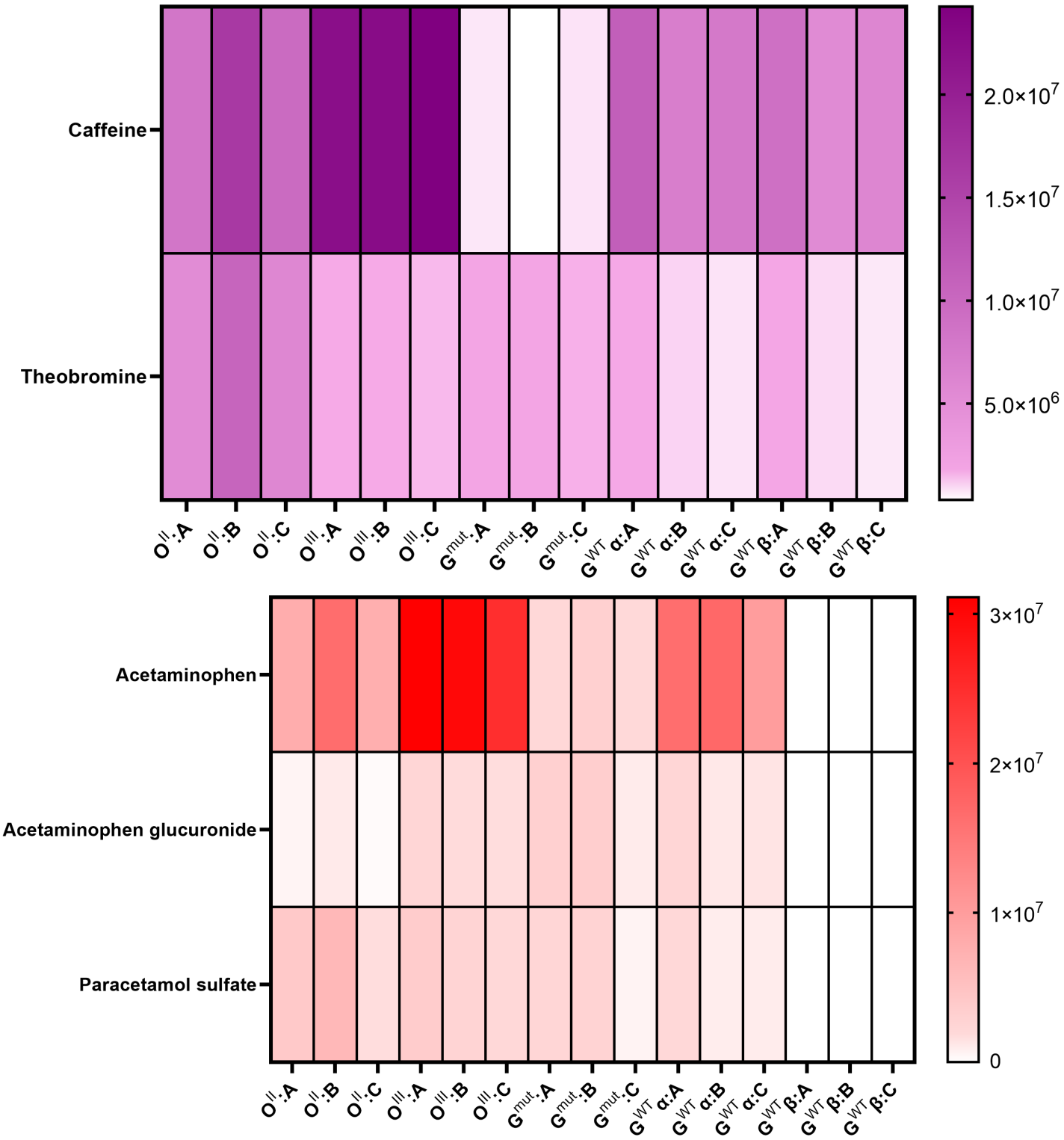

Fig 1. **Patient characteristics, intraoperative microdialysis set-up, planning.** (**A**) Five patients were included in this study, two with oligodendrogliomas, WHO grade II (O^{II}) or III (O^{III}), and three with glioblastomas (GBM). IDH status and molecular features are summarized, as available (see methods for details). Catheter placement into "Enhancing" tumor, non-enhancing ("FLAIR") tumor or "Brain" adjacent to tumor was defined via intraoperative neuronavigation. *No further molecular characterization performed. **(B**) Intraoperative photograph demonstrating placement of three 100 kDa catheters per patient during microdialysate collection, depicting the pumps, catheters, and collection vials. (**C-E)** Trajectory views obtained while planning catheter placement on the Stealth Neuronavigation platform demonstrate the intended microdialysis catheter trajectory (blue line) toward the desired placement site for each 10mm microdialysis membrane (yellow box) within enhancing (**C,** Catheter A) and non-enhancing tumor (**D**, Catheter B) in addition to relatively normal brain adjacent to tumor (**E**, Catheter C).

Fig 2. **Elevated D-2-Hydroxyglutarate in IDH-mutant tumor microdialysate.** (**A**) D2-HG concentration was quantified in microdialysate recovered from 10µL of microdialysate from each of 3 catheters per patient via targeted metabolomics (LC-MS). Microdialysate samples are color-coded according to the patient's tumor status as IDH-mutant (blue) vs IDH-WT (Red). Symbol shape indicates placement location (see legend). CSF was recovered from the surgical field in three patients and evaluated for D2-HG concentration (green X). (**B**) Untargeted metabolomic analysis was performed on 20µL microdialysate from the same aliquot as used for targeted metabolomics. 2-Hydroxyglutarate (2-HG) peak areas obtained via untargeted metabolomic analysis do not discriminate between D2-HG and L2-HG. These were correlated to the sum total of D and L-2HG measured via targeted metabolomic analysis. (**C**) Principal Component Analysis was performed, based on the full complement of 181 named metabolites detected in each of 15 catheters. Microdialysate samples from each catheter are shown, categorized by samples from patients IDH-mutant and IDH-wild type tumors. The first two principal components are shown on the x and y axes, respectively.

Fig 3. Reproducible individualized metabolic signatures from enhancing tumor versus brain microdialysate. For each patient with an enhancing tumor (n=3), metabolites were ranked by fold difference between abundance in catheters A versus C. The top 35 enhancing tumor-associated metabolites for each patient was then used for Enrichment Analysis. (A) Enrichment analysis plot demonstrating positive enrichment for the top 35 metabolites in GBM^{mut} catheter A vs C in the ranked metabolite list of $GBM^{WT}2$ catheter A vs C. (B) Enrichment Analysis output plot demonstrating negative enrichment for the top 35 metabolites from GBM^{mut} catheter A vs C in the ranked gene list comparing $GBM^{WT}2$ catheter C vs A. (C) Normalized enrichment scores (NES) were calculated for the top 35 "Enhancing" tumor and "Brain"- associated metabolites in the ranked metabolite lists for each patient. metabolites for each A versus C metabolite list. Enrichment for metabolite sets from prior publications were also evaluated. (D/E) Top metabolites contributing to the leading edge of enrichment in enhancing tumor (D) and brain (E) were found based on their presence in both other GBM patient samples when each patient's catheters were compared to one another for positive (D) and negative (E) enrichment. Bolded

metabolites were present in the leading edge of enrichment for all possible comparisons between each patient.

Fig 4. Microdialysate samples cluster by patient groups. (**A**) Pearson Correlation Map clustered by 181 metabolites present in all samples. (-1: negatively correlated, 1: positively correlated). (**B**) Pearson correlation map clustered by 15 samples, with a minimal correlation of 0.7 and maximal correlation of 1. (**C**) Principal Component Analysis was performed for the 15 catheter samples grouped by patient; the top two principal components (2D projection) are shown on the x and y axes, respectively. (**D**) Sparse Partial Least Squares-Discriminant Analysis (sPLS-DA) for the 15 catheter samples grouped by patient; first two components shown.

Fig 5. Microdialysate-based tumor phenotypes. (A, B) Heatmaps for the top 25 metabolites differentiating phenotypes across all 12 tumor microdialysate samples, including catheters in enhancing tumor and non-enhancing (FLAIR) tumor, based on IDH-mutant versus IDH-WT **(A)**, or α versus β metabolic phenotype (**B**). (**C-D**) Volcano plots depict the relative fold change (x-axis) and significance (based on t-test; y axis) for metabolites between groups based on (**C**) IDH-status and (**D**) metabolic phenotypes α versus βphenotypes.

Fig 6. Phenotypes α and β are distinct, but with preserved biomarkers. (**A**) Heatmap for the top 25 metabolites separating α-phenotype tumors and β-phenotype tumors from brain. (**B, C**) Volcano plots depict relative fold change (x-axis) and significance (based on t-test; y axis) separating (**B**) α phenotype tumor (n=4) from the brain adjacent to tumor (n=3) and β phenotype tumor (n=8) from brain adjacent to tumor (n=3). Colored metabolites are those meeting threshold criteria of (FC>2, p<0.05). (**D**) Venn Diagram of the most significant metabolites in phenotypes $\boldsymbol{\alpha}$ versus brain and β versus brain comparisons. For β Phenotype, an additional 45 metabolites met criteria (FC>2, p<0.05) but were omitted to maintain readability. The complete list of metabolites meeting criteria and their respective FC and p values are provided in supplemental table 4.

Fig. 7. Intra-operatively administered drugs detected in microdialysate. Untargeted metabolic data yielded peak areas for (**A**) Levetiracetam (Keppra), **(B)** cefazolin (Ancef), and **(C)** mannitol/sorbitol. Red box = drug not administered.

Supp Figure 1. Pathway Enrichment Analysis for Each Patient. Pathway enrichment analysis based on pathways from KEGG was conducted by comparing Catheter A to Catheter C for each patient and determining the normalized enrichment score for the most significantly enriched pathways at p<0.05 for all patients.

Supp Fig 2. Heat map for top 15 metabolites across phenotypes.
Throughout FC analyses, 15 metabolites were consistently identified as conserved metabolites between metabolic phenotypes α and β. Relative levels of each of the 15 metabolites were compared to one another for all 15 catheter samples using a heat map.

Supp Fig 3. Relative peak areas of caffeine, acetaminophen, and their metabolites. Relative peak area levels of caffeine and its metabolite, theobromine, and acetaminophen and its metabolites, acetaminophen glucuronide and paracetamol sulfate, were compared to one another across all 15 catheter samples.